Dewetting-induced collapse of hydrophobic particles

X. Huang, C. J. Margulis, and B. J. Berne*

Department of Chemistry and Center for Bimolecular Simulation, Columbia University, New York, NY 10027

A molecular dynamics study of the depletion of water (drying) around a single and between two hydrophobic nanoscale oblate plates in explicit water as a function of the distance of separation between them, their size, and the strength of the attraction between the plates and the water molecules is presented. A simple macroscopic thermodynamic model based on Young's law successfully predicts drying between the stacked plates and accounts for the free-energy barriers to this drying. However, because drying around a single plate is not macroscopic, a molecular theory is required to describe it. The data are consistent with the rate-determining step in the hydrophobic collapse of the two plates being a large-scale drying fluctuation, characterized by a free-energy barrier that grows with particle size.

Hydrophobicity is important in chemistry, biochemistry, and biology. The self-organization of amphiphiles into micelles and membranes (1), capillary evaporation (2–5), protein folding (6–11), and gas solubility are just a few examples of processes governed by hydrophobic hydration and hydrophobic interaction. It is now recognized that small-scale hydrophobic solutes hydrate differently than large ones. Small solutes (argon, methane, etc.) can fit into the hydrogen-bond network of water without destroying hydrogen bonds (12–17), whereas larger hydrophobic solutes, starting with molecules as small as neopentane (18), induce reorganization of water such that OH groups point into the surface, thus producing dangling hydrogen bonds (19). Simulations have shown that on hydrophobic faces of proteins, certain hydrophobic residues do not break neighboring water hydrogen bonds, whereas other residues do (10) such that protein faces can be heterogeneously "small" or "large." Also, as first surmised by Stillinger (15), it is now appreciated that large, strongly hydrophobic particles should induce a liquid–vapor-like interface. Recently, experimental evidence (20) of the existence of this molecular-size vapor layer around large paraffin-like molecules has been reported. This vapor layer is also predicted by the Lum–Chandler–Weeks theory (21, 22), but, to the best of our knowledge, no computer simulation involving explicit solvent has been able to observe thus far this phenomenon (i.e., the proximal water density less than the bulk density) around convex-shaped hydrophobic particles. [It has been observed in simulations of a drop of water confined in a spherical cavity in paraffin (23).] We report here an observation of this molecular-size vapor layer around nanosize objects dissolved in water (24) as obtained from our constant temperature and pressure molecular dynamics simulations.

In 1995, Wallqvist and Berne (25, 26) showed by simulation that, when two strongly hydrophobic plates (Gay–Berne ellipsoids) are brought together to a separation allowing more than one layer of water to fill the space between them, the water is expelled instead, a result already anticipated theoretically (27, 28). They also computed the potential of mean force for this system, which, as a result of the spontaneous drying, displays a very strong driving force for hydrophobic collapse (or aggregation). As we shall see, the exact number of water layers that will be expelled depends on the size of the plates. A sequence of papers by the Chandler group, using analytical theories and simulations, have provided an explanation of many of the important facets of hydrophobicity and drying including the role of drying in the kinetics of hydrophobic collapse (9, 11, 21, 22,

29–32). Others have addressed related issues (1, 5, 23, 26, 33–38). There is great interest in this (14) because, if, as has been suggested, dewetting must precede hydrophobic collapse for large hydrophobic solutes or for the folding or aggregation of globular proteins, then the kinetics of folding must account for this process. Of course it is possible that, when the attractive dispersion interactions between water and hydrophobes are included, dewetting might play a greatly reduced role.

We discuss our results in the context of a very simple macroscopic thermodynamic model based on Young's equation, which was shown valid for large hydrophobic particles (21). This model is found to give useful estimates of barriers to drying and wetting, to the critical distance for drying, and for the hydrophobic driving force for hydrophobic collapse, which becomes longer-ranged as the size of the hydrophobic plate is increased. We simulate the kinetics of collapse in our model system and observe from this trajectory that the rate-determining step is large-scale cooperative dewetting, a result consistent with earlier transition-path sampling simulations on lattice gas models (11). We also show that when solute–water attractive forces are included, the critical distance for dewetting is considerably reduced, as expected.

Simulation Methods and Simple Theory

The systems studied consist of one or two oblate ellipsoids in simple point charge (SPC) (24) water. We chose to use either a purely repulsive interaction or a full dispersion solute–solvent interaction that includes attractions. The full interaction is modeled by using the Gay–Berne potential (25) for the interaction between an ellipsoid and an oxygen atom of water.

$$U_{sw}^{(full)} = 4\varepsilon[(\sigma_0/(r - \sigma(\chi; v) + \sigma_0))^{12} - (\sigma_0/(r - \sigma(\chi; v) + \sigma_0))^6] \qquad [1]$$

The purely repulsive solute–solvent interaction is modeled as the repulsive part, $U_{sw}^{(rep)}$, of the Gay–Berne potential (25), which is given by first term on the right-hand side of Eq. **1**, where $\sigma(\chi; v)$ is an orientation-dependent Lennard–Jones diameter,

$$\sigma(\chi; v) = \sigma_\perp / \sqrt{(1 - \chi \cos^2 v)},$$

where $\chi = (\sigma_\parallel^2 - \sigma_\perp^2)/\sigma_\parallel^2$, $\sigma_\parallel$, and $\sigma_\perp$ are the axial ratio and lengths of the oblate ellipsoid along the major and minor axes, respectively, v is the angle between the major axes of the ellipsoid and the unit vector pointing from the center of the ellipsoid to water's oxygen atom, and $\sigma_0 = (\sigma_\perp^2 \sigma_\parallel)^{1/3}$. In the simulations we take $\varepsilon = 592.5$ cal/mol. One of the nice features of using Gay–Berne ellipsoids (25, 26, 39) for the plates is that one can increase the surface area of the plate by simply increasing its axial ratio without increasing their volume. Thus, one can study larger surface areas without the need to increase the number of water molecules as would be the case for spheres.

Classical molecular dynamics simulations were performed by using the RATTLE (40) algorithm to constrain the internal

CHEMISTRY

geometry of the water molecules and the particle–particle particle–mesh Ewald method (41, 42) to treat long-range electrostatic interactions. All simulations were performed at constant temperature (298.15 K) and pressure (1 atm [1 atm = 101.3 kPa]) with Nose–Hoover chain thermostats and an Andersen–Hoover-type barostat (43, 44) by using the program SIM (45), developed in our group.

To study the phenomenon of hydrophobic interaction, we simulated pairs of Gay–Berne ellipsoids of fixed $\sigma_\parallel = 3.1$ Å and of different $\sigma_\perp$ values ranging from 8 up to 13 Å. For each $\sigma_\perp$, a series of simulations with different separation D between the two ellipsoids were performed. For each D two simulations with different initial conditions were performed. The first type of initial condition corresponds to the plates separated by water at bulk density, and the second corresponds to the two plates separated by vapor. A box with 2,048 water molecules was first equilibrated for 150 ps, then the ellipsoids were introduced, and overlapping water molecules were removed. Water molecules in the intervening region between plates were removed in the second case. In both cases plates were kept at fixed positions in the laboratory frame, and production runs were 100 ps long. These simulations were done with both the full and repulsive solute–solvent potentials. We also study the role that weak attractive interactions play in the solvation of single nanosize hydrophobic objects (see *Results*).

In an attempt to study the dynamics of collapse, a constant temperature and pressure simulation was performed in which the minor axis of each plate was forced to remain parallel to the X–Y plane. The plates could only move along the z axis. The constraining potential $V_{pr}(r_i) = (1/2)k_{pr}(x_i^2 + y_i^2)$ was applied on two points along the major axis of each ellipsoid. Here, i labels each of the two points on the major axis of each ellipsoid. The major axis of the ellipsoids was chosen to be along the laboratory z axis. k_{pr} was chosen to be 500 kcal/Å^2. In addition, to prevent the plates from diffusing too far apart, a flat restraining potential was imposed to keep the plates closer than half the length of the box. The potential form for this restraint is given by

$$V_{dr}(r) = \begin{cases} k_{dr}(r - r_0)^6 & \text{for } r > r_0 \\ 0 & \text{for } r \le r_0 \end{cases} \qquad [2]$$

In this case, $k_{dr} = 1$ kcal/Å^6, r is the interplate distance, and r_0 was chosen to be 20 Å. For convenience the mass of each plate was chosen to be that of two argon atoms. After initial equilibration, the fictitious isothermal–isobaric dynamics was followed during a 30-ps production run before the plates came into close contact.

The following approximate simple macroscopic thermodynamic analysis provides a context for understanding the results of the computer simulations presented here (46–49). The grand potential of the liquid confined between the two plates is $\Omega_l = -PV + 2A_w\gamma_{wl}$, whereas the grand potential of the confined vapor is $\Omega_v = -P_vV + 2A_w\gamma_{wv} + A\gamma_{lv}$, where V is the volume of the confined region between the two plates, A_w is the corresponding contact area between the plates and the fluid, and A is the liquid–vapor interface area (5). Here we assume, for simplicity, that the vapor will occupy a cylindrical region instead of the "hourglass" region observed in our previous simulations (25). For two parallel circular disks of radius R_m separated by a distance D, $V = \pi R_m^2 D$, $A_w = \pi R_m 2$, and $A = 2\pi R_m D$. The change in grand potential accompanying the transition from liquid to vapor is

$$\Delta\Omega = \Omega_v - \Omega_l = (P - P_v)V - 2\Delta\gamma A_w + A\gamma_{lv}, \qquad [3]$$

where γ_{lv}, γ_{wv}, and γ_{wl} are the liquid–vapor, wall–vapor, and wall–liquid surface tensions, respectively, and

$$\Delta\gamma \equiv \gamma_{wl} - \gamma_{wv} = -\gamma_{lv}\cos\theta_c \qquad [4]$$

is Young's equation with θ_c being the contact angle for the liquid in contact with the wall of the plate. For a hydrophobic surface the contact angle is obtuse and $\Delta\gamma > 0$. From this it can be seen that $\Delta\Omega$ is a linear function of D. For D smaller than the critical separation D_c,

$$D_c = 2\Delta\gamma/((P - P_v) + b\gamma_{lv}/R_m), \qquad [5]$$

vapor between the disks is stable; however, for $D > D_c$, liquid between the disks is stable. Here b is a geometric factor that, for cylindrical disks, is $b = 2$. It is important to note that for small plate sizes (small R_m), D_c grows linearly with plate size. For macroscopic-size plates, drying should occur for very large separations. Below we will see that the barrier to drying will grow approximately as D^2 such that although the dry state may be the thermodynamically stable state, it may be difficult to achieve.

The approach discussed above can also be used to compute the change in free energy accompanying the creation of a cylindrical bubble of radius R based concentrically on the discs separated by D:

$$\Delta\Omega = 2\pi RD\gamma_{lv} - [2\Delta\gamma - (P - P_v)D]\pi R^2. \qquad [6]$$

This provides a nucleation-theory approach to the problem. It is clear from this equation that for $D < D_0 \equiv 2\Delta\gamma/(P - P_v)$, $\Delta\Omega$ will rise from 0 to a maximum of $\Delta\Omega_c = \pi\gamma_{lv}^2D^2/((P - P_v)(D_0 - D))$ at $R = R_c = \gamma_{lv}D/((P - P_v)(D_0 - D))$ and then decreases as a function of R until at $R = R_m$ it starts increasing again. Thus, even if the vapor is stable, a system starting with liquid between the plates ($R = 0$) will have to cross a free-energy barrier to reach equilibrium in which there is a cylindrical bubble (with $R = R_m$). There are three possible regimes: (*i*) $D < D_c < D_0$; (*ii*) $D_c < D < D_0$; and (*iii*) $D_c < D_0 < D$. In case *i* the stable state is a vapor ($\Delta\Omega(R_m) < \Delta\Omega(R = 0)$), in case *ii* it is a liquid ($\Delta\Omega(R_m) > \Delta\Omega(R = 0)$), and in case *iii* there is no barrier separating liquid and vapor. Thus in case *i* the barrier for the liquid-to-vapor transition is smaller than the vapor-to-liquid transition, and in case *ii* the reverse is true. We can use the above theory to determine these rates and to rationalize the observations from the simulation. This "back-of-the-envelope" model also gives a prediction for the potential of mean force between the plates of radius R_m:

$$\Delta\Omega(D) = \begin{cases} [\pi R_m^2(P - P_v) + 2\pi R_m\gamma_{lv}](D - D_c) & \text{for } D \le D_c \\ 0 & \text{for } D > D_c \end{cases}$$

$$[7]$$

From this it follows that once the plates are close enough for drying to take place, the mean hydrophobic driving force for collapse will be

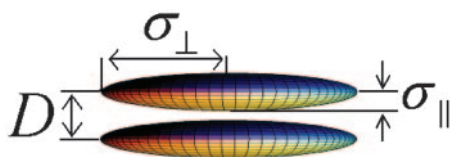$$\bar{F} = [\pi R_m^2(P - P_v) + 2\pi R_m\gamma_{lv}] \qquad [8]$$

and will grow with plate size and with surface tension. Moreover, this driving force will become very long-range, because D_c grows linearly with plate size.

The theory discussed above can be modified for the ellipsoidal disks. In the case of an oblate ellipsoid (two equal minor axes $\sigma_\perp$ and one major axis $\sigma_\parallel$) as described in Fig. 1 we find

$$V = \pi\sigma_\perp^2 D - 4\pi\sigma_\perp^2\sigma_\parallel/3;$$

$$A_w = \pi\sigma_\perp^2 + (\pi\sigma_\perp\sigma_\parallel^2/\sqrt{\sigma_\perp^2 - \sigma_\parallel^2})\ln[(\sigma_\perp + \sqrt{\sigma_\perp^2 - \sigma_\parallel^2})/\sigma_\parallel]; \text{ and}$$

$$A = 2\pi\sigma_\perp D.$$

Fig. 1. Schematic diagram for the two-ellipsoid system in which parameters D, $\sigma_\perp$, and $\sigma_\parallel$ are defined.

Substituting these expressions for A_w, A, and V into Eq. **3**, setting $\Delta\Omega = 0$ for $R = R_m$, above, and solving for D gives

$$D_c = ((4/3)\pi\Delta P\sigma_\parallel\sigma_\perp^2 - 2\gamma_{lv}A_w\cos\theta_c) / (2\pi\gamma_{lv}\sigma_\perp + \pi\Delta P\sigma_\perp^2).$$

[9]

These simple thermodynamic arguments, based on Young's equation, show that macroscopic hydrophobic objects dissolved in water should expel the solvent trapped between them if brought closer than a characteristic critical distance D_c that depends on geometry and thermodynamic properties. Although thermodynamics clearly predicts the existence of this drying transition, the free-energy barrier to cross from the wet to the dry state could be very large, effectively freezing the system in a metastable state (31, 37). This free-energy barrier is responsible for the phenomenon of cavitation-induced hysteresis, which has been observed (50, 51) experimentally in surface-force measurements. Do drying transitions and the predictions of macroscopic thermodynamics still hold when systems are of nano- or subnanometer dimensions? This is relevant, for example, to assess whether drying-induced collapse is what drives the process of protein folding.

Results

Molecular dynamics simulations were performed to test the predictions of the macroscopic theory (*Simulation Methods and Simple Theory*) to determine the effect of attractive solute–solvent interactions on the dewetting around single nanoscale particles and to study how the fluctuations leading to dewetting between the plates affect the kinetics of hydrophobic collapse. To test the validity of Eq. **9**, we simulated Gay–Berne ellipsoids (25) in SPC water (see Fig. 1 for a definition of the parameters and distances) both for full (Eq. **1**) and for the purely repulsive Gay–Berne solute–solvent potential between SPC (24) water molecules and the ellipsoids. The length of the ellipsoid along the C_∞ axis is set to be a constant ($\sigma_\parallel \equiv 3.1$ Å); however, the length along the minor C_2 axes, $\sigma_\perp$, is varied to scale the lateral size of the hydrophobic object.

Under the conditions of the simulation, $\Delta P \approx 1$ atm, $\sigma_\parallel = 3.1$ Å, and $\gamma_{lv} = 72.1$ mJ/m². Because the contact angle θ of SPC water with these hydrophobic ellipsoids is unique, the critical distance D_c given by Eq. **9** only depends on $\sigma_\perp$. To test this equation, two simulations with different initial conditions were launched for each given interplate distance: one simulation with water filling the space in between plates ("wet" initial conditions) and a second one where water molecules were removed from this region ("dry" initial conditions).

Results for different interplate distances all with the same plate size ($\sigma_\perp = 13$ Å) are displayed in Fig. 2 *C*, *B*, and *D* with interplate distances D of 14, 16, and 18 Å, respectively. These observations are very similar to the dewetting observed in two plates immersed in an Lennard–Jones fluid (32). In the simulation of $D = 14$ Å with wet initial conditions given in Fig. 2*C*, we observed that a layer of vapor developed next to each plate in <10 ps. Large capillary wave fluctuations along the two liquid–vapor interfaces occurred. After 60 ps, the two vapor layers coming from each side finally touched, and a vapor tube
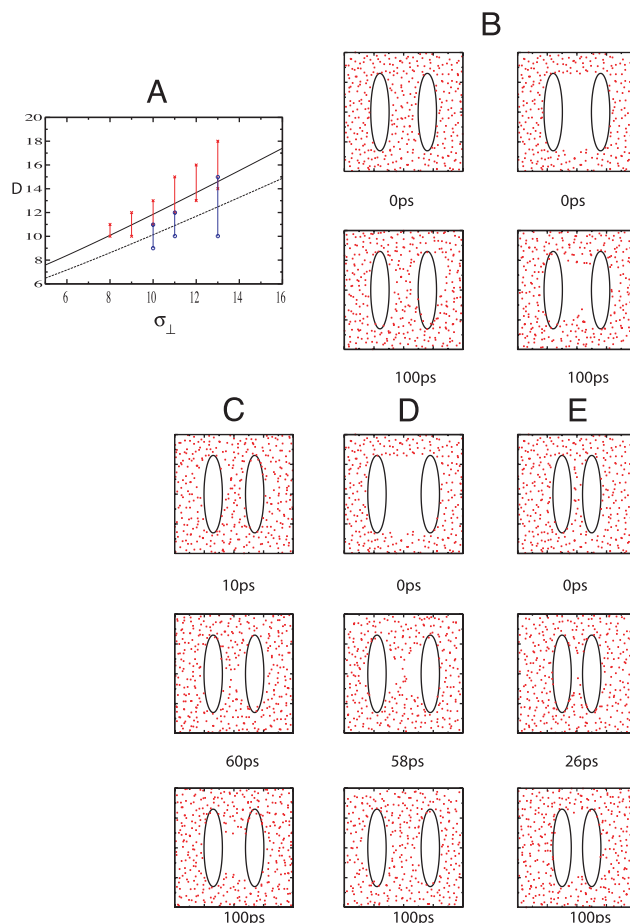
Fig. 2. (*A*) The relationship between the critical distance D_c and the size of the plate $\sigma_\perp$ is shown for the purely repulsive (red) and full Gay–Berne (blue) potentials. For each $\sigma_\perp$, the error bar perpendicular to the $\sigma_\perp$ axis indicates a lower and upper bound for the critical distance D_c. The solid black (purely repulsive case) and dashed (full Gay–Berne potential) lines were obtained by fitting the simulation data to Eq. **9**. Units of D and $\sigma_\perp$ are in ångstroms. (*B*) Two-dimensional projection of the two-plate system in SPC water. Red dots correspond to the position of water oxygen atoms. Water molecules obscuring the solute (i.e., those water molecules in which the absolute value of the Y coordinate, which in this case is perpendicular to the projection plane, is >4 Å) have been removed. The size of the plate is $\sigma_\perp = 13$ Å and $\sigma_\parallel = 3.1$ Å, and the interplate distance is $D = 16$ Å. The black line corresponds to the k_BT equipotential surface for the water–solute interactions. Water interacts with the ellipsoids through the purely repulsive Gay–Berne potential. (*Left*) System with wet initial conditions. (*Right*) System with dry initial conditions. Both axes span a range of 40 Å. (*C*) Same as *B Left* with $D = 14$ Å. (*D*) Same as *B Right* with $D = 18$ Å. (*E*) Same as *B Left* but using, in this case, the full potential interaction in Eq. **1** and with interplate distance $D = 10$ Å.

formed. Between 60 and 100 ps, the vapor grew to finally fill up almost the whole region between the two plates taking on the shape of an hourglass. A very similar hourglass-like pattern for capillary drying was observed in the umbrella-sampling Monte Carlo studies of Leung *et al.* (4) and in the Monte Carlo simulations of simple lattice gas models (2, 31). When dry initial conditions were deployed instead, the system remained dry for the whole duration of our 100-ps simulation, although large thermal fluctuations due to capillarity waves were observed, and the vapor once again organized into an hourglass shape. From these simulations we conclude that, although between two and three layers of water could fit in the intervening region between these plates, the dry state is thermodynamically stable and a phase separation occurs.

CHEMISTRY

The opposite situation arises when the interplate separation D was increased to 18 Å; in this case, the wet state was thermodynamically stable, as can be appreciated from Fig. 2D. In Fig. 2D the system starts from dry initial conditions, and capillarity waves at the liquid–vapor interface intrude from opposite sides and finally join at 60 ps, after which liquid fills up the interplate volume. When the system starts from wet initial conditions, it remains wet for the rest of our 100-ps run.

The results for an intermediate separation of 16 Å shown in Fig. 2B are interesting because they approximately correspond to a separation of D_c. In this case we observe a hysteresis phenomenon [see Lum–Chandler–Weeks theory for a discussion of hysteresis (21)]. Starting from wet initial conditions the system remains wet at least for 100 ps, whereas starting from dry initial conditions the system remains dry. Large fluctuations are observed in both simulations as if the initially dry system was about to become wet and vise versa. The simple theory shown in *Simulation Methods and Simple Theory* predicts that the barriers to go from wet to dry or dry to wet for a separation of $D \approx D_c$ are considerably larger than to go from the less stable to the more stable state for either $D > D_c$ or $D < D_c$, thus explaining the observed hysteresis.

A series of simulations using the full Gay–Berne potential (Eq. 1) with plates of size $\sigma_\perp = 13$ Å and different interplate separation D were performed following the same procedure as described above. A drying transition is observed in systems with $D \leq 10$ Å, compared with $D \leq 14$ Å for the repulsive interaction. This can be appreciated in Fig. 2E. When $D \geq 15$ Å, the wet state becomes thermodynamically stable. As we see from these simulations, attractive interactions between water and plates do not eliminate the drying transition, but dewetting only occurs when the plates are much closer and only a single layer of water molecules fit in the intervening region. We note from Eqs. 4 and 5 that D_c will decrease if the contact angle θ_c decreases, which it surely does when attractive forces are turned on. Thus the less hydrophobic the particle is, the smaller will be the critical distance for dewetting. This causes us to wonder whether attractive electrostatic and dispersion interactions of water with the protein backbone and side chains will so reduce the critical distance that dewetting will cease to play an important role in protein folding and aggregation. The net effect of dewetting will also depend on the size of the hydrophobic region.

A similar analysis was carried out for a set of plate pairs of different sizes $\sigma_\perp$ to obtain in each case a lower and upper bound limit to the critical separation D_c. For the particular plate size described above in the case of the purely repulsive Gay–Berne interaction, 14 Å $< D_c <$ 18 Å. Fig. 2A shows the relation between the critical distance D_c and the size of the plates $\sigma_\perp$. These curves were generated by fitting Eq. 9 to reproduce the simulation data. The contact angle observed from our simulation is $\approx 180°$ for the purely repulsive Gay–Berne potential, whereas results using the full Gay–Berne potential in Eq. 1, which includes weak attractions between the plates and water, results in a contact angle of $\approx 148°$. These results are compatible with typical hydrocarbon contact angles reported in literature (4). For example, for water–paraffin, the contact angle is 140°. Our findings suggest that Eq. 9 derived from macroscopic thermodynamics approximately holds for microscopic systems of the size of proteins and nanostructures. The dewetting transition can thus be understood from the perspective of simple macroscopic arguments based on Young's equation.

From the discussions above we see that two or three water layers confined between hydrophobic plates can be expelled due to hydrophobic interaction. For larger plates, theory predicts that the number of water layers that can be ejected is proportional to the size of the plates. The loss of hydrogen-bond partners makes confined water thermodynamically unstable, and a drying transition occurs. How does attraction between water
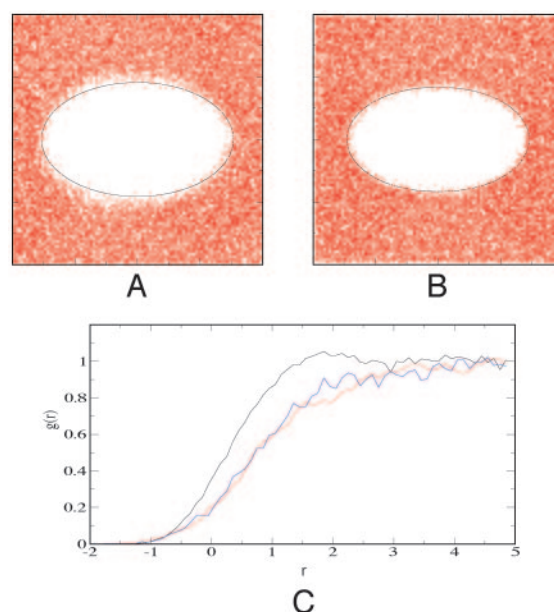
Fig. 3. (*A*) *Two-dimensional projection of 100 snapshots of the system collected during 100 ps of simulation. The size of the hydrophobic ellipsoid is* $\sigma_\parallel = 9.1$ Å *and* $\sigma_\perp = 15.3$ Å. *Water interacts with the plate through the purely repulsive Gay–Berne potential. Water molecules obscuring the solute have been removed as described for Fig. 2. The black line corresponds the solute–solvent* $k_B T$ *equipotential energy surface. Both axes span a range of 40 Å.* (*B*) *Same as A but using the full Gay–Berne potential in Eq. 1 instead.* (*C*) *Solute–oxygen distribution functions. Ellipsoidal shells are used to compute the distribution function: r is the distance (in ångstroms) along* $\sigma_\perp$, *and r = 0 Å corresponds to the* $k_B T$ *equipotential surface. The black line corresponds to the system interacting through the full Gay–Berne potential (see Eq. 1). In the case of the red and the blue lines, only the purely repulsive potential was used. The red line corresponds to the system being prepared by removing water molecules adjacent to a plate of size* $\sigma_\parallel = 9.1$ Å *and* $\sigma_\perp = 15.3$ Å. *The blue line was obtained by equilibrating a smaller ellipsoid of size* $\sigma_\parallel = 3.1$ Å *and* $\sigma_\perp = 9.3$ Å *and gradually allowing it to grow during 50 ps.*

and the hydrophobic plates affect these results? Do plate–water attractive interactions compensate for the loss of hydrogen bonds? Understanding this is crucial, because even the most hydrophobic regions in proteins have polarity and dispersion interactions with the solvent.

The Lum–Chandler–Weeks theory (21, 22) predicts that large nanosize hydrophobic solutes should display a depletion of solvent density in contact with their surface if water is close enough to the liquid–vapor coexistence line. However, in earlier work (25, 38), no such depletion was observed around fully repulsive Gay–Berne plates of size $\sigma_\perp = 9.3$ Å and $\sigma_\perp = 3.1$ Å.

To investigate whether a density depletion and/or vapor layer exists around single large hydrophobic objects in water at room temperature and pressure and verify that results were independent of initial conditions, two simulations were performed by using the purely repulsive solute–solvent form of the Gay–Berne potential. In the first case, a "vacuum" layer around the plate was created by removing water molecules adjacent to the plate. The system then was allowed to equilibrate for 100 ps by using constant pressure and temperature molecular dynamics with the algorithms described above. Subsequent 100-ps runs were used to collect the data displayed in Fig. 3A. Finally a 20-ps production run was used to compute the plate–oxygen density distribution function. The minor ($\sigma_\perp$) and major ($\sigma_\parallel$) axes of this ellipsoid were chosen to be 15.3 and 9.1 Å, respectively. In the second case, the system was first equilibrated by using a smaller ellipsoid ($\sigma_\perp = 9.3$ Å and $\sigma_\parallel = 3.1$ Å) for 50 ps. Then, during subsequent 50-ps runs, this small ellipsoid dissolved in water was allowed to

grow gradually to a size of $\sigma_\perp = 15.3$ Å and $\sigma_\parallel = 9.1$ Å. Subsequent 100-ps runs were used for equilibration, and finally a 20-ps production run was used to compute the plate–oxygen distribution function.

To study the role that weak attractive interactions play in the solvation of single nanosize hydrophobic objects, we determined the difference in water-density profile around this plate when the full Gay–Berne potential was used Eq. **1** as opposed to the purely repulsive Gay–Berne interaction. A single simulation was carried out with initial conditions being exactly the same as those described above for the first case of a single purely repulsive Gay–Berne plate dissolved in water in the previous paragraph.

We report here the observation of a molecular size vapor layer for plates of size $\sigma_\perp = 15.3$ Å and $\sigma_\perp = 9.1$ Å, as can be observed in Fig. 3*A*, a phenomenon predicted by the Lum–Chandler–Weeks theory (22). In Fig. 3*A*, 100 snapshots collected during 100 ps of a constant temperature and pressure molecular dynamics simulation are overlayed. The width of the vapor layer is ≈ 3 Å, which corresponds to the molecular diameter of a single water molecule. To test the validity of this result, we carried out two different protocols described in *Simulation Methods and Simple Theory*. In both cases the water-density distribution functions were, for all practical purposes, identical. We also investigated the case in which the full Gay–Berne potential was used. In Fig. 3*B*, 100 snapshots collected during 100 ps of a constant temperature and pressure molecular dynamics simulation were overlayed. A comparison between the density distribution functions obtained by using only the repulsive part of the Gay–Berne potential and that with the full interaction is displayed in Fig. 3*C*. From Fig. 3*C* it is easy to see that, although for both cases there seems to be a density depletion in contact with the plates, this depletion is much more pronounced in the case of the fully repulsive interaction. These distribution functions are remarkably similar to those obtained next to a liquid–vapor interface (52). We notice here that in the case of the full Gay–Berne interaction, $g(r)$ has a first peak with a maximum of 1.2 [similar peak heights have been observed in previous simulations (19)], whereas in the absence of attractions this first peak disappears and the distribution function grows monotonically from a value of zero inside of the plates to the corresponding bulk-density value. Interestingly, Wallqvist and Berne (25, 26) did not observe a vapor layer around single repulsive plates, perhaps because their plates were too small or because they used a different model of water (Reduced Effective Representation model instead of SPC).

From our foregoing results, we see that, depending on the size of the hydrophobic plate studied, vapor can be the thermodynamically stable phase in the intervening region. It is of interest to address the question of whether water will be collectively expelled before hydrophobic collapse such that collective drying becomes the rate-determining step in hydrophobic collapse. Alternatively, do single water molecules diffuse away as the plates approach each other? We performed a constant pressure and temperature molecular dynamics simulation of two Gay–Berne plates of size $\sigma_\perp = 13$ Å at an initial separation of 11 Å. Initially, water filled up the intervening region between plates. Plates were only allowed to move in the Z direction, that is, along their C_∞ axes. Because of the constraints imposed on the system, which are described in *Simulation Methods and Simple Theory*, the planes of the plates remained parallel to the X and Y laboratory axes. The only interaction potential coupling the plates was imposed to preclude them from drifting apart to distances larger than half of the box. Because this potential was essentially zero for all practical purposes, their motion was only driven by the solvent. We observed during the first 13 ps of simulation that the distance between plates consistently decreased at the same time as water left the intervening region. At this point a drying transition occurred even though two or three
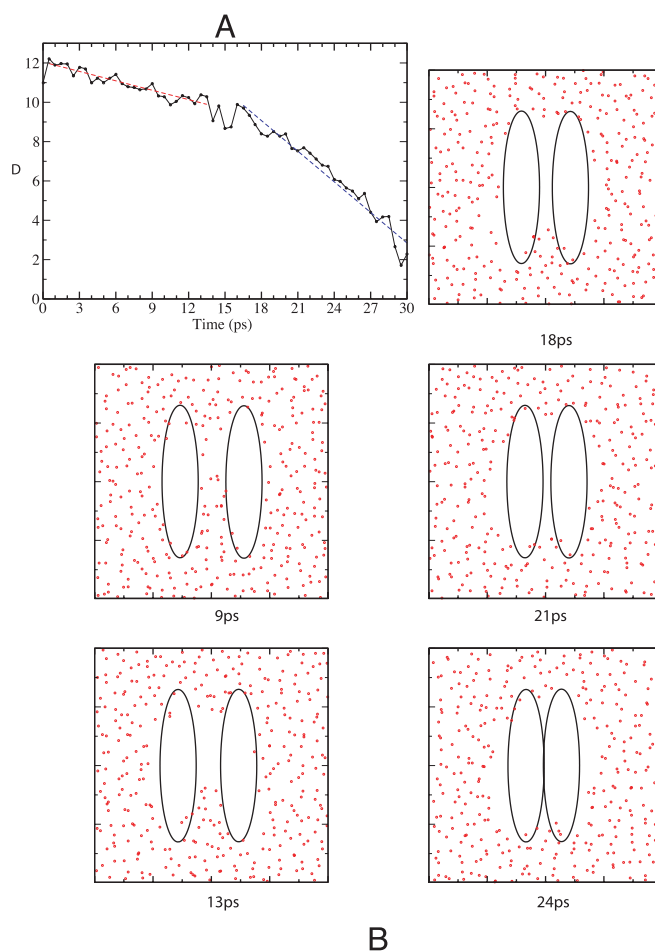
Fig. 4. (*A*) Interplate distance *D* (the distance between the centers of the two ellipsoids in ångstroms) as a function of time. The red fitted line corresponds to initial slope before drying transition, and the blue fitted line corresponds to final slope after drying transition. (*B*) Snapshots correspond to the time evolution of the system. Projections were constructed in the same way as described for Fig. 2. Plates were constrained such that they could only move along the direction of $\sigma_\parallel$. The initial interplate distance was $D = 11$ Å. Both axes span a range of 40 Å.

layers of water could be accommodated between the plates. As is to be expected, after this sudden drying transition, the driving force (see Eq. **8**) is very large, and therefore the hydrophobic plates immediately collapsed. The change in the speed of approach between the two plates before and after the drying transition can be appreciated in Fig. 4*A* from the difference in slope between the red (before the drying transition) and blue (after the drying transition) lines. This is consistent with experimental observations by Christenson and Claesson (50). Clearly, in this particular case, drying preceded collapse. Snapshots describing the time evolution of the system are shown in Fig. 4*B*.

Conclusions

We have shown, following up on the work of Wallqvist and Berne (25), that when two hydrophobic nanoscale oblate plates are brought closer together than a characteristic critical distance D_c, spontaneous drying takes place. In the present simulations, we study oblate ellipsoids of fixed $\sigma_\parallel$ but variable $\sigma_\perp$. From extensive simulations we show that: (*i*) The critical distance, D_c, grows nearly linearly with $\sigma_\perp$ (see Fig. 2*A*) as predicted by the macroscopic theory, but D_c for the full potential lies below that of the purely repulsive potential, results consistent with macroscopic theory based on Young's equation. (*ii*) For fixed inter-

plate separations smaller than the critical distance, dynamics following the initial preparation of a wet state led to drying (after bubble nucleation), and dynamics following an initial dry state stayed dry. No hysteresis was observed. However, near the critical separation, a dry initial state stayed dry and a wet one stayed wet, showing marked hysteresis. The macroscopic theory accounts for these observations by predicting much higher barriers for the critical separation than for other separations. Note that Leung *et al*. (4), using open ensemble Monte Carlo simulations and umbrella sampling, recently estimated this activation barrier for water confined within weakly attractive infinite walls to be $\Delta\Omega \approx 10k_BT - 20k_BT$. (*iii*) The dynamics of plates separated initially ($<D_c$) is shown in Fig. 4 *A* and *B*. Hydrophobic collapse of the two plates is observed to take place only after a cooperative large-scale drying fluctuation. Somewhere between 9 and 13 ps, a bubble starts, nucleates, and grows by 18 ps, thereby dewetting the interplate region. After this, the strong hydrophobic force leads to a collapse of the plates by 24 ps. It can be seen from Fig. 4*A* that between 0 and 17 ps the plates slowly approach each other at a speed of 0.16 Å/ps, whereas between 18 and 30 ps they approach each other with a speed of ≈0.52 Å/ps. It is important to note that constant temperature and pressure molecular dynamics is "fictitious dynamics." (*iv*) In the case of large oblate plates, surface dewetting is observed (Fig. 3), but this effect is much smaller when attractive solute–solvent forces are included. Fig. 3*C* shows how weak attractive forces affect the water-density profile around the plates for both the full and purely Gay–Berne potential. The macroscopic theory used to describe the interplate-dewetting simulations is not applicable to depletion around single plates, because this occurs over molecular distances (21). (*v*) The potential of mean force between plates close enough ($D < D_c$) to undergo a drying transition is expected to be very large. The simple macroscopic model gives a prediction for this embodied in Eq. **7**, with an accompanying driving force for hydrophobic collapse in Eq. **8**.

The very approximate macroscopic theory was found to qualitatively predict all of our findings with the exception of the formation of a microscopic vapor layer around single plates. A microscopic theory is required for this as well as a more quantitative and detailed treatment of dewetting between the plates. Because the introduction of attractive forces reduces the critical separation and the thickness of the vapor layer around single plates, it is of considerable interest to study dewetting in the hydrophobic-induced aggregation of domains in multidomain proteins. Such studies will clarify whether cooperative hydrophobic dewetting plays an important role in protein aggregation and folding.

1. Hummer, G., Garde, S., Garcia, A. E. & Pratt, L. R. (2000) *Chem. Phys.* **258,** 349–370.
2. Luzar, A. & Leung, K. (2000) *J. Chem. Phys.* **113,** 5836–5844.
3. Leung, K. & Luzar, A. (2000) *J. Chem. Phys.* **113,** 5845–5852.
4. Leung, K., Luzar, A. & Bratko, D. (2003) *Phys. Rev. Lett.* **90,** 65502.
5. Lum, K. & Luzar, A. (1997) *Phys. Rev. E Stat. Phys. Plasmas Fluids Relat. Interdiscip. Top.* **56,** 6283–6286.
6. Li, B., Alonso, D. O. V., Bennion, B. J. & Dagget, V. (2001) *J. Am. Chem. Soc.* **123,** 11991–11998.
7. Mountain, R. D. & Thirumalai, D. (2003) *J. Am. Chem. Soc.* **125,** 1950–1957.
8. Wallqvist, A., Covell, D. G. & Thirumalai, D. (1998) *J. Am. Chem. Soc.* **120,** 427–428.
9. Huang, D. M. & Chandler, D. (2000) *Proc. Natl. Acad. Sci. USA* **97,** 8324–8327.
10. Cheng, Y. & Rossky, P. J. (1998) *Nature* **392,** 696–699.
11. TenWolde, P. R. & Chandler, D. (2002) *Proc. Natl. Acad. Sci. USA* **99,** 6539–6543.
12. Pratt, L. R. & Chandler, D. (1977) *J. Chem. Phys.* **67,** 3683–3704.
13. Chandler, D. (2002) *Nature* **417,** 491.
14. Ball, P. (2003) *Nature* **423,** 25–26.
15. Stillinger, F. H. (1973) *J. Solution Chem.* **2,** 141–158.
16. Pangali, C., Rao, M. & Berne, B. J. (1979) *J. Chem. Phys.* **71,** 2982–2990.
17. Pangali, C., Rao, M. & Berne, B. J. (1979) *J. Chem. Phys.* **71,** 2975–2981.
18. Huang, X., Margulis, C. J. & Berne, B. J. (2003) *J. Phys. Chem. B*, in press.
19. Lee, C. Y., McCammon, J. A. & Rossky, P. J. (1984) *J. Chem. Phys.* **80,** 4448–4455.
20. Jensen, T. R., Jensen, M. O., Reitzel, N., Balashev, K., Peters, G. H., Kjaer, K. & Bjornholm, T. (2003) *Phys. Rev. Lett.* **90,** 86101.
21. Lum, K., Chandler, D. & Weeks, J. D. (1999) *J. Phys. Chem. B* **103,** 4570–4577.
22. Huang, D. M. & Chandler, D. (2002) *J. Phys. Chem. B* **106,** 2047–2053.
23. Wallqvist, A., Gallicchio, E. & Levy, R. M. (2001) *J. Phys. Chem. B* **105,** 6745–6753.
24. Berendsen, H. J. C., Postma, J. P. M., van Gunsteren, W. F. & Hermans, J. (1981) in *Intermolecular Forces*, ed. Pullman, B. (Reidel, Dordrecht, The Netherlands), pp. 331–342.
25. Wallqvist, A. & Berne, B. J. (1995) *J. Phys. Chem.* **99,** 2893–2899.
26. Wallqvist, A. & Berne, B. J. (1995) *J. Phys. Chem.* **99,** 2885–2892.
27. Bérard, D. R., Attard, P. & Patey, G. N. (1993) *J. Chem. Phys.* **98,** 7236–7244.
28. Patey, G. N. (1996) *Ber. Bunsen Ges. Phys. Chem.* **100,** 885–888.
29. TenWolde, P. R., Sun, S. X. & Chandler, D. (2001) *Phys. Rev. E Stat. Phys. Plasmas Fluids Relat. Interdiscip. Top.* **65,** 011201.
30. Huang, D. M., Geissler, P. L. & Chandler, D. (2001) *J. Phys. Chem. B* **105,** 6704–6709.
31. Lum, K. & Chandler, D. (1998) *Int. J. Thermophys.* **19,** 845–855.
32. Bolhuis, P. G. & Chandler, D. (2000) *J. Chem. Phys.* **113,** 8154–8160.
33. Paulaitis, M. E. & Pratt, L. R. (2002) *Adv. Protein Chem.* **62,** 283–310.
34. Pratt, L. R. (2002) *Annu. Rev. Phys. Chem.* **53,** 409–436.
35. Hummer, G., Garde, S., Garcia, A. E., Paulaitis, M. E. & Pratt, L. R. (1998) *J. Phys. Chem. B* **102,** 10469–10482.
36. Talanquer, V. & Oxtoby, D. W. (1995) *J. Chem. Phys.* **103,** 3686–3695.
37. Bratko, D., Curtis, R. A., Blanch, H. W. & Prausnitz, J. M. (2001) *J. Chem. Phys.* **115,** 3873–3877.
38. Rick, S. W. & Berne, B. J. (1997) *J. Phys. Chem. B* **101,** 10488–10493.
39. Gay, J. & Berne, B. J. (1981) *J. Chem. Phys.* **74,** 3316–3319.
40. Andersen, H. C. (1983) *J. Comput. Phys.* **521,** 24–34.
41. Zhou, R., Harder, E., Xu, H. & Berne, B. J. (2001) *J. Chem. Phys.* **115,** 2348–2358.
42. Luty, B. A., Tironi, I. G. & van Gunsteren, W. F. (1995) *J. Chem. Phys.* **103,** 3014.
43. Martyna, G. J., Klein, M. L. & Tuckerman, M. E. (1992) *J. Chem. Phys.* **97,** 2635–2643.
44. Martyna, G. J., Tobias, D. J. & Klein, M. L. (1994) *J. Chem. Phys.* **101,** 4177–4189.
45. Stern, H., Xu, H., Harder, E., Rittner, F., Pavesse, M. & Berne, B. J. (2000) SIM, Molecular Dynamics Simulation Program (Dept. of Chemistry and Center for Bimolecular Simulation, Columbia Univ., New York).
46. Tolman, R. C. (1949) *J. Chem. Phys.* **17,** 118–127.
47. Rice, O. K. (1947) *J. Chem. Phys.* **15,** 333–335.
48. Gibbs, J. W. (1928) *Collected Works* (Longmans Green and Company, New York), Vol. 1.
49. Lewis, G. N. & Randall, M. (1961) *Thermodynamics* (McGraw–Hill, New York).
50. Christenson, H. K. & Claesson, P. M. (1988) *Science* **239,** 390–392.
51. Parker, J. L., Claesson, P. M. & Attard, P. (1994) *J. Phys. Chem.* **98,** 8468–8480.
52. Taylor, R. S., Dang, L. X. & Garret, B. C. (1996) *J. Phys. Chem.* **100,** 11720–11725.